

## Multispectral electromagnetic shielding using ultra-thin metal-metal oxide decorated hybrid nanofiber membranes

Dayong He<sup>1,12</sup>, Nan Zhang<sup>1,2,12</sup>, Aamir Iqbal<sup>3,4</sup>, Yuying Ma<sup>1</sup>, Xiaofeng Lu<sup>1</sup>, Zhen-An Qiao<sup>1,5</sup>, Ji-Hong Yu<sup>5</sup>, Hongbo Xu<sup>6</sup>, Wei Wang<sup>6</sup>, Rui Zhao<sup>7</sup>, Xiaofeng Li<sup>8</sup>, Zhiqiang Zhou<sup>9</sup>, Changxian Jin<sup>10</sup>, Chong Min Koo<sup>3,4,11</sup> & Ce Wang<sup>12</sup>

Lightweight shielding materials that can protect devices against undesirable multispectral electromagnetic waves are critical in electronic, medical, military, and aerospace applications. However, the existing shielding materials are heavyweight and work only in a narrow frequency-range. In this work, we developed metal-metal oxide Ag-WO<sub>3</sub> decorated polymeric nanofiber hybrid membranes with versatile multispectral electromagnetic shielding abilities for practical applications. The Ag-WO<sub>3</sub> hybrid provides multiple functions, such as excellent metallic conductivity provided by silver, high photoelectric effect and low thermal conductivity arising from the high atomic number in WO<sub>3</sub>, and strong infrared energy absorbing capability caused by a designed Schottky barrier interface between Ag and WO<sub>3</sub>. Additionally, the nanofibrous hybrid membrane structure provides high surface area, good air permeability, and robust mechanical strength and durability. These highly conductive, lightweight, ultrathin, and flexible membranes exhibit efficient microwave electromagnetic interference shielding of 92.3 dB at a thickness of ~42 μm in 8–26.5 GHz frequency range, 0.75–0.5 emissivity for near- to far-field infrared bands, and 32.03% attenuation for X-rays of 30 keV at 0.24 mm thickness, indicating their potential for shielding against large-scale multispectral electromagnetic waves from low-frequency microwaves to high-frequency X-rays.

<sup>1</sup> College of Chemistry, Alan G. MacDiarmid Institute, Jilin University, 130012 Changchun, People's Republic of China. <sup>2</sup> Jilin Province Product Quality Supervision and Inspection Institute, 2699 Yiju Road, 130012 Changchun, People's Republic of China. <sup>3</sup> Materials Architecturing Research Centre, Korea Institute of Science and Technology (KIST), Seoul 02792, Republic of Korea. <sup>4</sup> Division of Nano & Information Technology, KIST School, University of Science and Technology, Seoul 02792, Republic of Korea. <sup>5</sup> State Key Laboratory of Inorganic Synthesis and Preparative Chemistry, College of Chemistry, Jilin University, 130012 Changchun, People's Republic of China. <sup>6</sup> MIIT Key Laboratory of Critical Materials Technology for New Energy Conversion and Storage, School of Chemistry and Chemical Engineering, Harbin Institute of Technology, 150001 Harbin, People's Republic of China. <sup>7</sup> Division of Ionizing Radiation, National Institute of Metrology, China, 100029 Beijing, People's Republic of China. <sup>8</sup> State Key Laboratory of Organic-Inorganic Composites, College of Materials Science and Engineering, Beijing University of Chemical Technology, 100029 Beijing, People's Republic of China. <sup>9</sup> Changchun Tongyuan Hospital, 130021 Changchun, People's Republic of China. <sup>10</sup> Jilin Zhenliang Scientific and Technology Company, 130000 Changchun, People's Republic of China. <sup>11</sup> KU-KIST Graduate School of Converging Science and Technology, Korea University, Seoul 02841, Republic of Korea. <sup>12</sup> These authors contributed equally: Dayong He, Nan Zhang. ✉email: [koo@kist.re.kr](mailto:koo@kist.re.kr); [cwang@jlu.edu.cn](mailto:cwang@jlu.edu.cn)

The electromagnetic spectrum consists of radio waves, microwaves, infrared (IR) rays, visible light, ultraviolet light, X-rays, and gamma rays, which are classified depending on their frequency or wavelength. Multispectral man-made and/or natural electromagnetic waves (EMWs) promote rapid advances in electronic, medical, military, and aerospace devices. However, these advancements are accompanied by electromagnetic interference (EMI), which causes several side effects, such as device malfunctions and threats to human health. Therefore, shielding materials that can effectively block the unwanted EMWs are essential<sup>1–5</sup>.

Recently, demand for lightweight multispectral shielding materials has increased exponentially owing to the introduction of high-tech devices operating on multispectral EMWs. For example, smart electronics and telecommunication satellites function in the dual-band spectrum of microwaves and infrared radiations<sup>6</sup>. X-ray diagnostic instruments in hospitals use microwaves and X-rays<sup>7</sup>. Aerospace vehicles endure and struggle with multiple spectral waves including microwaves, IR, and X-rays coming from the Sun<sup>7</sup>. Unfortunately, currently available shielding materials are mostly designed for single-band EMWs, and do not meet multispectral shielding requirements. This is because each band in the EMWs has a different attenuation mechanism (see the shielding mechanism for different bands of EMWs in Supplementary Figs. 1 and 2)<sup>1,8–11</sup>. Microwave shielding materials should exhibit high electrical conductivity, dielectric permittivity, and magnetic permeability for Faraday shielding<sup>1,12–15</sup>. Incident microwaves are effectively reflected after striking the conductive shield containing dense charge carriers or their energy is absorbed within the shield via ohmic and polarization losses<sup>1</sup>. Metals, which are the most conductive materials, are believed to be the best candidates for microwave shielding and have been used for this purpose for decades<sup>16–19</sup>. However, their heavyweight, high cost, and weak corrosion resistance limit their applications in advanced high-tech mobile and aerospace equipment. Moreover, their multispectral shielding ability is still unexplored. As an alternative, highly conductive carbon materials<sup>20–22</sup>, and 2D MXenes<sup>1,23–25</sup>, provide extremely high shielding efficiency due to their excellent electrical conductivities<sup>26</sup>, but these materials are high cost and also suffer from poor mechanical properties. Fabrication of their polymeric composites improved their mechanical properties along with tunable shielding<sup>27–30</sup>. X-rays, which consist of high-energy photons, are useful for medical diagnosis and crystallography. However, overexposure to such radiation can damage live human cells. The attenuation of X-rays requires metals with high atomic numbers for a strong photoelectric effect or Compton scattering. At present, lead-based materials are the material-of-choice against X-rays, however, their toxicity, environmental instability, and heavyweight necessitate the development of lead-free X-ray shielding materials<sup>7</sup>. Meanwhile, IR shielding or camouflage technology in military and security applications requests shielding materials with low infrared emissivity and low thermal conductivity<sup>31</sup>. According to Kirchhoff's law of thermal radiation for opaque materials<sup>32</sup>, a low IR emissivity is primarily achieved by a high reflectivity, which in turn is dependent on the electrical conductivity. A low thermal conductivity is a key to inhibit heat transfer in a material. In this context, due to their large thermal conductivity, highly conductive metals are not suitable for IR shielding. Although multilayered structures composed of an electrically conductive metal layer and a low thermally conductive semiconducting or insulating layer offer both low IR emissivity and effective thermal conductivity, unfortunately, these materials require high thicknesses to be effective<sup>32</sup>. Therefore, due to the different attenuation mechanisms in each EMW frequency band,

designing lightweight multispectral shielding materials is extremely challenging.

Herein, we present lightweight metal–metal oxide (Ag-WO<sub>3</sub>) decorated polymeric nanofiber hybrid membranes with multispectral electromagnetic shielding capabilities. Based on different principles, effectively shielding of multispectral EMWs could be achieved by the hybrid nanofibrous membrane, ranging from microwave of longer wavelength (lower frequency), and IR ray with intermediate wavelength, to X-ray with shorter wavelength (higher frequency). Electrospinning of polymeric nanofibers composed of polyacrylonitrile (PAN) and polyurethane (PU), followed by electroless deposition of Ag-WO<sub>3</sub> on the nanofibers resulted in a flexible and lightweight PAN-PU nanofiber membrane decorated with Ag-WO<sub>3</sub> (PP@AW). Silver was used as an electrically conductive material<sup>5,33–37</sup>, while semiconducting WO<sub>3</sub> which has a low thermal conductivity, catalyzed the formation of metallic silver on the nanofibers<sup>38–40</sup>. Tungsten, which has a high atomic number, resulted in a strong photoelectric effect<sup>41–43</sup>. Moreover, the Schottky junction effect in electron-rich Ag-WO<sub>3</sub> hybrids and the high specific surface area of the hybrid nanofiber membranes synergistically enhanced IR shielding. The fabricated lightweight hybrid nanofiber membranes also showed excellent flexibility and durability against bending fatigue. The synthetic approach is simple that all steps are based on proven technology (electrospinning and electroless deposition) and all chemical reactions take place at room temperature, making the nanofiber membranes cost-effective feasible for large-scale industrial production. Besides, the fabricated membranes can be adapted to the electromagnetic wave shielding of various bands including X-, Ku-, and K-bands. This finding will lead to the discovery of new lightweight multispectral shielding materials for next-generation flexible electronic, medical, military, and aerospace applications.

## Results and discussion

**Synthesis and characterization of Ag-WO<sub>3</sub>-coated polymeric nanofiber hybrid membranes.** Synthesis process of nanofiber hybrid membranes mainly consists of three steps, as illustrated in Fig. 1m. First, PAN-PU nanofibrous membrane doped with AgNO<sub>3</sub> (PP@AgNO<sub>3</sub>) were prepared through electrospinning technique. Second, a microwave-assisted reaction was applied on the PP@AgNO<sub>3</sub> membranes to obtain Ag seed-anchored membranes (PP@Ag seed). Finally, the PAN-PU@Ag-WO<sub>3</sub> (PP@AW) hybrid membranes were prepared through a simple electroless deposition process on the PP@Ag seed membrane with the help of seed effects, a series of membranes with a different feed ratio of Ag and WO<sub>3</sub> precursor was prepared. Ag-WO<sub>3</sub> coated polymeric nanofiber hybrid membranes were prepared by electrospinning a mixture of PAN-PU (PP) and AgNO<sub>3</sub> followed by electroless co-deposition of Ag and WO<sub>3</sub> on the electrospun nanofiber membrane (a detailed fabrication process can be found in the “Methods” section). The electrospun PP@AgNO<sub>3</sub> hybrid membranes showed a uniform intertwined nanofibrous morphology with a smooth surface and a diameter of ~150 nm (Fig. 1a). Chemical reduction of adsorbed Ag<sup>+</sup> ions on PP@AgNO<sub>3</sub> membranes by microwave irradiation produced polymeric nanofiber membranes coated with 20–30 nm Ag nanoparticle (PP@Ag seed) (Fig. 1b). Subsequently, Ag and WO<sub>3</sub> were uniformly coated on the Ag nanoparticle seeds in the PP@Ag membrane using an electroless plating solution containing AgNO<sub>3</sub>, Na<sub>2</sub>WO<sub>4</sub>, and hydrazine as a reducing agent, to obtain Ag-WO<sub>3</sub>-coated PP membranes (PP@AW24) (Fig. 1c; “24” in the sample name PP@AW24 denotes a 2:4 feed molar ratio of AgNO<sub>3</sub> to Na<sub>2</sub>WO<sub>4</sub> precursors in the plating solution).

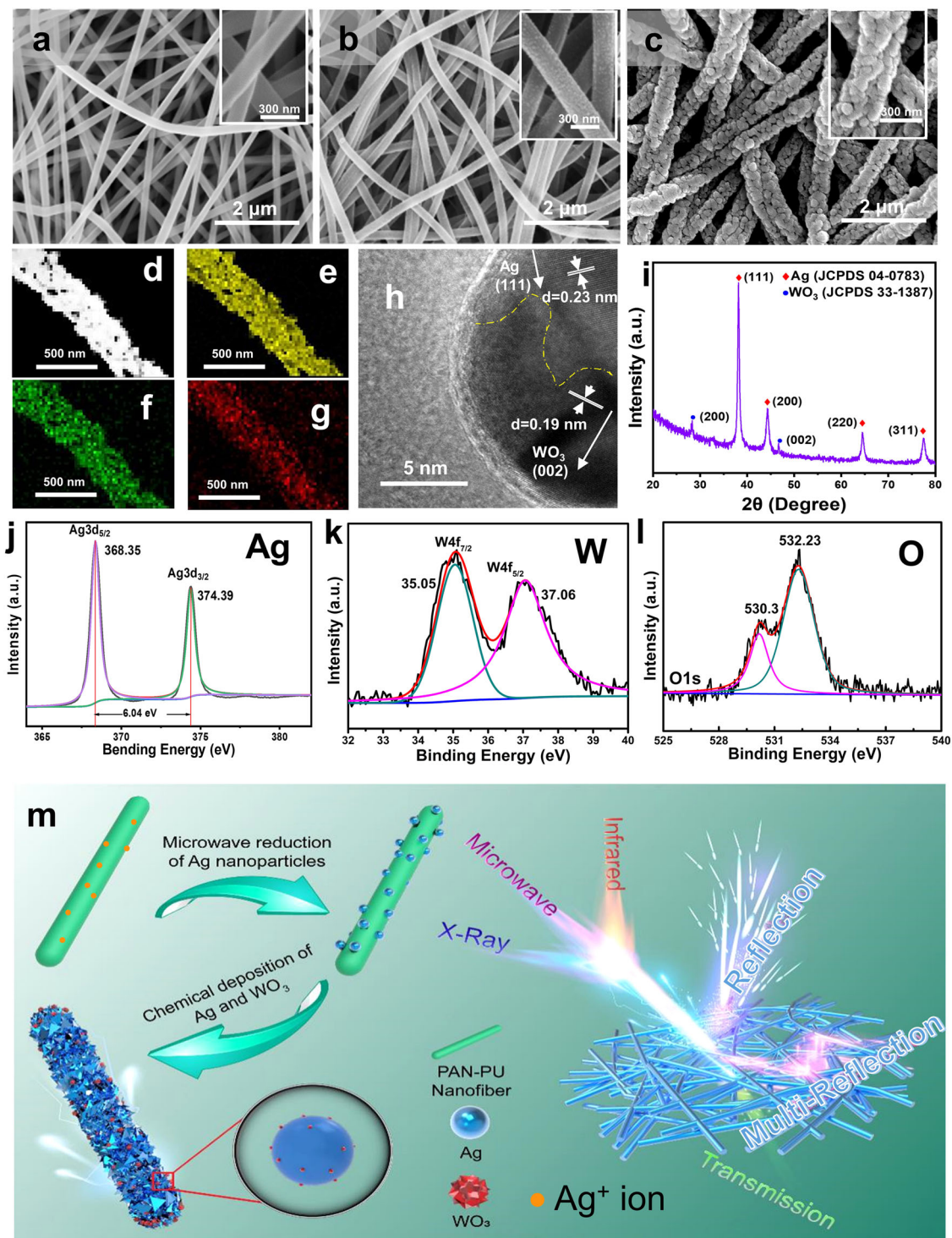


**Fig. 1** Electron microscopy and spectroscopy characterization and preparation procedure of the hybrid membranes. FE-SEM images of **a** the as-spun PP/AgNO<sub>3</sub> nanofiber membrane, **b** PP@Ag seed membrane, and **c** PP@AW24 hybrid membrane. The inset images in **b** and **c** are their corresponding magnified SEM images. **d–g** STEM image (Z-contrast) and EDX element mapping images of Ag, W, and O in Ag/WO<sub>3</sub> nanofibers, respectively. **h** HRTEM image of PP@AW24 hybrid membrane. **i** XRD pattern of the PP@AW24 hybrid membrane. High-resolution XPS spectra of **j–l** Ag 3d, W 4f, and O 1s in PP@AW24 hybrid membrane. **m** Schematic illustration of the preparation procedure for the PP@AW hybrid membrane.

Energy-dispersive X-ray (EDX) analysis and elemental mapping of Ag, W, and O revealed that Ag and WO<sub>3</sub> were homogeneously deposited on the nanofibers (Fig. 1d–g and Supplementary Fig. 3). High-resolution transmission electron microscopy (HRTEM) image clearly showed lattice fringes (marked in white) of the Ag and WO<sub>3</sub> nanocrystals, corresponding to the (111) plane of Ag (JCPDS 04-0783) and (002) plane of

WO<sub>3</sub> (JCPDS 33-1387) (Fig. 1h). X-ray diffraction (XRD) pattern in Fig. 1i confirmed (111), (200), (220), and (311) peaks of the Ag nanocrystals and (200) and (002) peaks of WO<sub>3</sub>, which are consistent with the TEM results.

The surface compositions of individual elements in the PP@AW24 hybrid membrane were analyzed by X-ray photoelectron spectroscopy (XPS). Figure 1j exhibits two energy bands at

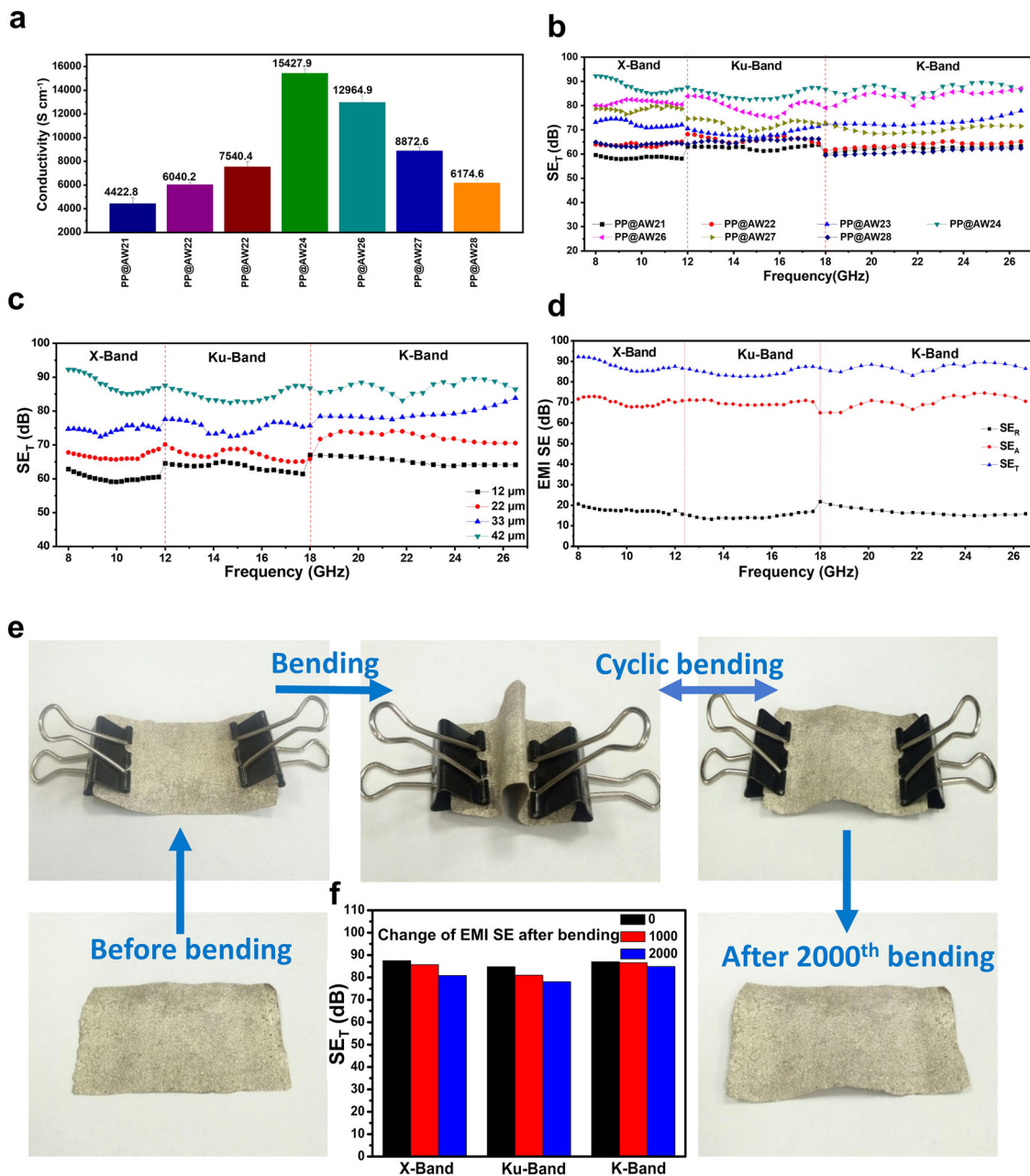


**Fig. 2** Electrical conductivity, microwave shielding, and mechanical properties of PP@AW hybrid membranes. **a** Electrical conductivity of PP@AW hybrid membranes with different Ag/W ratios. **b** Microwave shielding effectiveness  $SE_T$  of PP@AW hybrid membranes with different Ag/W ratios. **c**  $SE_T$  of PP@AW24 hybrid membranes with different thicknesses. **d** Shielding performance of PP@AW24 hybrid membranes, the detailed contribution of  $SE_A$  and  $SE_R$  to total  $SE_T$  and their dependence on frequency. **e** Mechanical flexibility and durability of hybrid membranes. The PP@AW24 membrane was flexible enough to retain its structural integrity even after 2000 bending cycles and there were negligible changes in its  $SE_T$  values as shown in **f**.

368.3 and 374.3 eV, which are characteristic of metallic Ag<sup>0</sup>. Peaks corresponding to W 4f<sub>7/2</sub> and 4f<sub>5/2</sub> were centered at 35.1 and 37.1 eV, respectively, corresponding to W<sup>6+</sup> species (Fig. 1k), whereas the broad peak corresponding to O 1s split into two peaks at 530.3 eV (WO<sub>3</sub>) and 532.23 eV (C=O in PAN and PU) (Fig. 1l). As shown in the Raman spectra, the characteristic peaks of the W<sup>6+</sup>=O stretching mode of terminal oxygen atoms at 946 cm<sup>-1</sup>, O–W–O bending vibrations at 240 and 370 cm<sup>-1</sup>, and WO<sub>3</sub> lattice vibrations at 116 cm<sup>-1</sup>, respectively, support the successful formation of Ag–WO<sub>3</sub> metal–metal oxide hybrid particles on the surfaces of the fabricated polymeric nanofibers (Supplementary Fig. 4).

The morphology and electrical conductivity of the fabricated PP@AW membranes were dependent on precursor composition and reaction time. As the molar ratio of AgNO<sub>3</sub> to Na<sub>2</sub>WO<sub>4</sub> increased from 2:1 to 2:8, the electrical conductivity of the membranes initially increased to a maximum (at a molar ratio of 2:4), and then gradually decreased (Fig. 2a). The high conductivity value observed at a molar ratio of 2:4 can be attributed to the fact that the highest coating thickness was achieved under these conditions; this observation could be confirmed from nanofiber diameter (Supplementary Fig. 5). Elemental composition in the fabricated PP@AW membranes is given in Supplementary Table 1, indicating that the

PP@AW24 sample was observed with the highest alloy content among all the samples (77.45%), which may be the reason for its highest conductivity. As the molar ratio of AgNO<sub>3</sub> and Na<sub>2</sub>WO<sub>4</sub> in the synthesis process greatly affects the resulting membranes, we propose that as the content of Na<sub>2</sub>WO<sub>4</sub> increases up to 2:4, more Ag nanoparticles can be co-deposited on the silver seeds. However, when the ratio is higher than 2:4, the co-deposition reaction tends to occur in the solution rather than on the surface of the nanofiber due to the increased concentration of WO<sub>4</sub><sup>2-</sup> in the solution. It means that the reaction of heterogeneous nucleation dominates, where the role of silver seed becomes less obvious, and as a result, the alloy content in the resultant hybrid nanofiber decreases. The obtained nanofibers exhibited a similar millet nanostructure morphology and all hybrid nanofiber membranes exhibited densities lower than 1 g cm<sup>-3</sup>, indicating their huge potential in lightweight shielding applications. Deposition time in the synthesis process also affects the electrical properties of the nanofiber hybrid membrane. As the deposition time increased from 5 to 30 min, the thickness of the Ag-WO<sub>3</sub> coating layer on the PP@AW24 membranes increased, leading to a gradual increase in the electrical conductivity values from 2152 S cm<sup>-1</sup> to 15,427.9 S cm<sup>-1</sup> (Supplementary Figs. 6 and 5). The elemental composition of the fabricated PP@AW membranes is listed in Supplementary Table 2. It is important to note that a uniform coating of Ag-WO<sub>3</sub> on the polymeric nanofibers relies on the successful co-deposition reaction of Ag and WO<sub>3</sub> constituents during the electroless plating process, since the WO<sub>3</sub> deposited on nanofibers catalyzes and stimulates the deposition of metallic Ag<sup>44</sup>. Only Na<sub>2</sub>WO<sub>4</sub> could not produce a uniform PP@WO<sub>3</sub> hybrid membrane in the absence of AgNO<sub>3</sub> (Supplementary Fig. 8a). Similarly, without Na<sub>2</sub>WO<sub>4</sub> content, AgNO<sub>3</sub> alone could not yield uniform PP@Ag membranes (Supplementary Fig. 8b).

#### Microwave shielding characteristics of PP@AW membranes.

Figure 2b illustrates the shielding effectiveness (SE) of the fabricated membranes in a wide microwave frequency window ranging from X-band (8–12.4 GHz) and Ku-band (12–18 GHz) to K-band (18–26.5 GHz). It can be seen that the total shielding effectiveness (SE<sub>T</sub>) value depends on the Ag/W molar ratio in the hybrid membranes. The most conductive membrane, PP@AW24, exhibited the highest SE<sub>T</sub> of 92.3 dB at a thickness of ~42 μm, emphasizing the influence of electrical conductivity on the shielding effectiveness. This shielding performance of PP@AW24 membrane is comparable to the current state-of-the-art two-dimensional (2D) Ti<sub>3</sub>C<sub>2</sub>T<sub>x</sub> MXene<sup>1</sup>. Interestingly, all the fabricated hybrid membranes exhibited the SE<sub>T</sub> values greater than 60 dB, at a comparable thickness of 40–42 μm. Their shielding performance was also dependent on the Ag-WO<sub>3</sub> deposition time. For a fixed Ag/W ratio of 2:4 (PP@AW24), as the deposition time increased from 5 to 30 min, the SE<sub>T</sub> values increased linearly from 30.9 to 92.27 dB at 8 GHz at comparable thickness values (Supplementary Fig. 9). These results are attributed to the thickness of Ag/WO<sub>3</sub>-coating layer on the nanofiber, as a thicker conductive layer increased the electrical conductivity of the hybrid membrane.

The SE values also depend on the thickness of the hybrid membranes, as the intensity of the microwaves attenuates exponentially with the propagation length. The SE<sub>T</sub> value of 63.1 dB measured for PP@AW24 at 12 μm thickness increased up to 92.27 dB with increasing thickness to 42 μm (Fig. 2c). It should be noted that the PP@AW hybrid membranes showed an absorption dominant shielding mechanism (Fig. 2d). This result is ascribed to the highly porous structure of the hybrid membranes. In general, the porous structure of a shielding

material strengthens the phenomenon of internal multiple reflections, thus improving its absorption shielding ability<sup>23,45</sup>.

Additionally, the fabricated PP@AW hybrid membranes exhibited excellent mechanical flexibility and strength against repeated bending and folding fatigue (Fig. 2e). Even after 1000 and 2000 bending cycles, the structural integrity of the PP@AW24 membrane was well maintained without any noticeable degradation in electrical conductivity and microwave shielding properties (Fig. 2f and Supplementary Fig. 10). The hybrid membranes also revealed a very high air permeability of 1.995 mm s<sup>-1</sup> owing to their porous structure and low density of < 1.0 g cm<sup>-3</sup>.

#### X-ray absorption characteristics of PP@AW membranes.

The PP@AW hybrid membranes are expected to be beneficial in radiological protection from X-rays and gamma rays, especially in the design of lightweight and lead-free aprons for individual protection. Two parameters, viz. attenuation ratio and mass-attenuation coefficient ( $\mu/\rho$ ) were introduced to evaluate the attenuation capability of the PP@AW membranes (see the corresponding details in Supplementary Methods). X-ray attenuation depends on the energy of radiations of the source and sample thickness. Figure 3a shows the ability of PP@AW24 membranes to attenuate X-rays of various energies at different thicknesses. At the same radiation energy, the attenuation ratio increased with an increase in membrane thickness, which could be explained by the formula:

$I/I_0 = e^{-\mu x}$  where  $I$ ,  $I_0$ ,  $\mu$ , and  $x$  represent the penetrating and incident dose of X-rays, linear attenuation coefficient, and sample thickness, respectively. Meanwhile, their shielding ability decreased with an increase in the radiation energy, at a fixed thickness of 0.24 mm, the attenuation ratio was 32.03% with low-energy X-ray (30 keV) when compared with a value of 5.1% at 100 keV.

Interestingly, as shown in Fig. 3b, despite its porous structure and low density, PP@AW24 hybrid membrane exhibited much larger ( $\mu/\rho$ ) values than a neat Al foil over a wide X-ray energy window, shielding abilities of the metal foils were collected in our previous work<sup>46</sup>. In addition, the ( $\mu/\rho$ ) values of PP@AW24 membranes were comparable to those of neat heavy metal foils such as pure silver and lead, outperforming lead foil at radiation energies of 48 and 65 keV.

Theoretically, the interaction of photons with matter results in a photoelectric effect and Compton scattering, which determine the X-ray-attenuating ability of a material<sup>40–42,47</sup>. Co-deposited Ag-WO<sub>3</sub> hybrids with a high specific surface area (44.43 m<sup>2</sup> g<sup>-1</sup>, confirmed by the N<sub>2</sub> adsorption-desorption isotherms and the BET surface area, and provided in Supplementary Fig. 11) can provide more disordered extranuclear hybridized orbitals and extranuclear electrons, which can improve interactions between the fabricated membranes and incident X-ray radiations<sup>48,49</sup>. The probability of the photoelectric effect is related to  $Z^3/E^3$ , where  $Z$  is the atomic number of the absorbing element and  $E$  is photon energy<sup>50</sup>. The excellent shielding performance of the hybrid membranes can be mainly attributed to the hybrid Ag-W structure. The quantum effect of silver nanoparticles on the surface of polymeric nanofiber membranes could weaken the binding between Ag and W nuclei and electrons outside these nuclei. This increases electronic cloud density outside the nucleus, overlaps or crosses the orbits, and increases the probability of a photoelectric effect, as confirmed by past studies<sup>48–50</sup>.

Currently, lead-based aprons are being used for protection against X-rays, however, these are unsafe and heavy, which make them uncomfortable for use over long periods of time<sup>41</sup>. In contrast, PP@AW membranes exhibit a good shielding

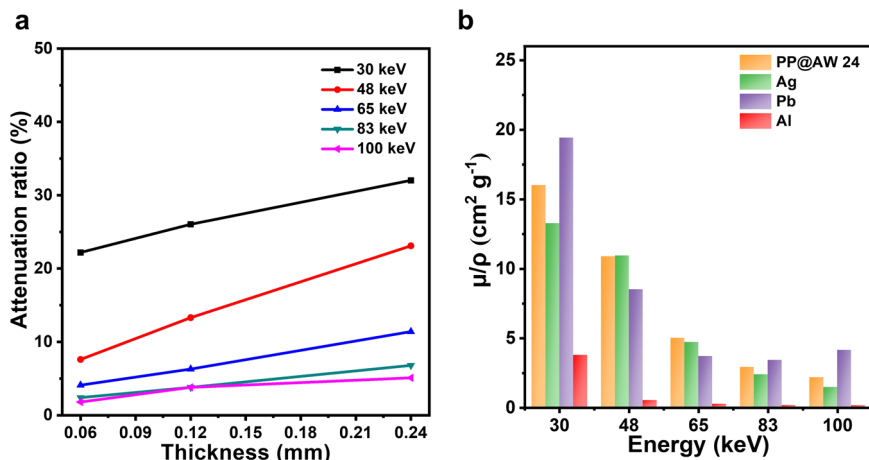


**Fig. 3 X-ray shielding properties.** **a** X-ray attenuating properties of PP@AW24 membranes with respect to thickness. **b** Comparison of mass-attenuation coefficients of PP@AW24 membranes (0.24 mm thickness) and Ag, Pb, and Al foils (0.15 mm thickness).

performance along with excellent safety, lightweight characteristics, mechanical flexibility and durability, and air permeability, and hence can be considered as potential candidates to replace lead-rubber aprons for X-ray protection and shielding in practical applications.

**IR shielding characteristics of PP@AW membranes.** IR shielding or camouflage materials should ideally have a low IR emissivity to isolate a target from IR radiation or reduce its energy before reaching a target. In other words, IR shielding materials should have a low energy-absorption rate with a certain level of thermal insulation to reduce heat absorption at the target surface, which prevents the target from radiating too much energy in the thermal infrared band.

According to Kirchhoff's law of thermal radiation for opaque objects, material emissivity can be evaluated by measuring its reflection coefficient<sup>32</sup>.

The camouflage performance of PP@AW membranes was directly monitored by measuring changes in its temperature using a FLIR ONE infrared imager (Fig. 4a, b). Cotton clothes were used as a reference. When clothes and PP@AW membranes were placed on a human body for 60 min, the temperature of the clothes was 34.8 °C, and these values were close to the temperature of the human body. In contrast, the PP@AW membranes showed an improved IR shielding ability with temperatures of 30.5, 28.0, and 29.9 °C for PP@AW22, PP@AW24, and PP@AW27, respectively. Figure 4c–e shows the changes in the IR emissivity of PP@AW membranes in near (2.5–8 μm), medium (8–14 μm), and far-infrared bands (14–20 μm), respectively. As described earlier, infrared emissivity was calculated by measuring the reflection coefficient. PP@AW22 exhibited a lower IR emissivity (<0.3) in the far-infrared band than PP@AW24 and PP@AW27. This indicates that our lightweight, safe, PP@AW membranes have great potential in practical applications of IR camouflage materials. The camouflage performance and low IR emissivity ensure the effectivity of as-prepared nanofibrous membranes protecting any sort of target object, as schematically presented in Supplementary Fig. 1, proving its application in camouflage against infrared reconnaissance equipment and reducing infrared interference.

To understand IR shielding mechanism of the PP@AW hybrid membranes, the energy band diagram of Ag and WO<sub>3</sub> in the Ag-WO<sub>3</sub> Schottky contact were calculated via Ab initio quantum chemistry methods (Fig. 4f, g, and Supplementary Methods). Work functions of pure Ag and WO<sub>3</sub> were found to be 4.3 and 2.54 eV,

respectively (Fig. 4h). Therefore, electrons flow from the semiconductor to the metal (Fig. 4i)<sup>51,52</sup>. The formation of a Schottky junction causes electrons in WO<sub>3</sub> to cross-over to the metallic silver, and subsequently, their Fermi levels are flattened<sup>1,53</sup>. Thus, more carriers in WO<sub>3</sub> can be excited by infrared radiation, resulting in energy attenuation and finally complete absorption. Moreover, the lower thermal conductivity of WO<sub>3</sub> resists the flow of heat towards the devices, thus ensuring their lower temperature. It is well-known that the electromagnetic shielding ability of a material is highly dependent on its type and structure; thus, a sufficiently large amount of Ag-WO<sub>3</sub> on the surface of multilayered membranes results in a low scattering by enabling the destructive interference of multiple reflections between layers. In addition, this also facilitates a high absorption and low emission of IR radiation<sup>1,54</sup>. Importantly, the differences in electromagnetic wave-attenuation mechanisms result in dissimilarities in infrared and microwave shielding performances. Therefore, despite its marginally lower electrical conductivity, PP@AW22 showed lower IR emissivity than PP@AW24. This can be attributed to the higher electron transfer efficiency in Schottky junctions of PP@AW22 owing to its better-infrared excitation efficiency. These results provide insights regarding the development of optimized multi-band electromagnetic shielding materials.

## Conclusion

We developed Ag-WO<sub>3</sub>-coated polymeric nanofiber hybrid membranes for multispectral electromagnetic shielding in a wide frequency-range spanning microwaves, infrared rays, and X-rays. Nanofibrous morphology of fabricated membranes facilitated a large surface area and porous network with excellent mechanical strength and durability. Improved electrical conductivity due to the addition of Ag nanoparticles, and porous structure of the hybrid membranes enhanced their absorption dominant microwave shielding properties. The unique Schottky barrier effect between Ag and WO<sub>3</sub> facilitated electron transfer from semiconductor to metal, thus effectively attenuating IR radiations. In addition, the lightweight and air permeable nanofibrous hybrid membranes can be comfortably worn by users when compared to heavy and toxic lead-rubber aprons. Therefore, our ultrathin and flexible electrospun PP@AW hybrid membranes, which exhibit a superior lightweight multispectral shielding performance, are promising for practical application in next-generation electronic, medical, military, and aerospace technologies. Finally, we expect this strategy to direct and inspire further research on multi-functional shielding materials.

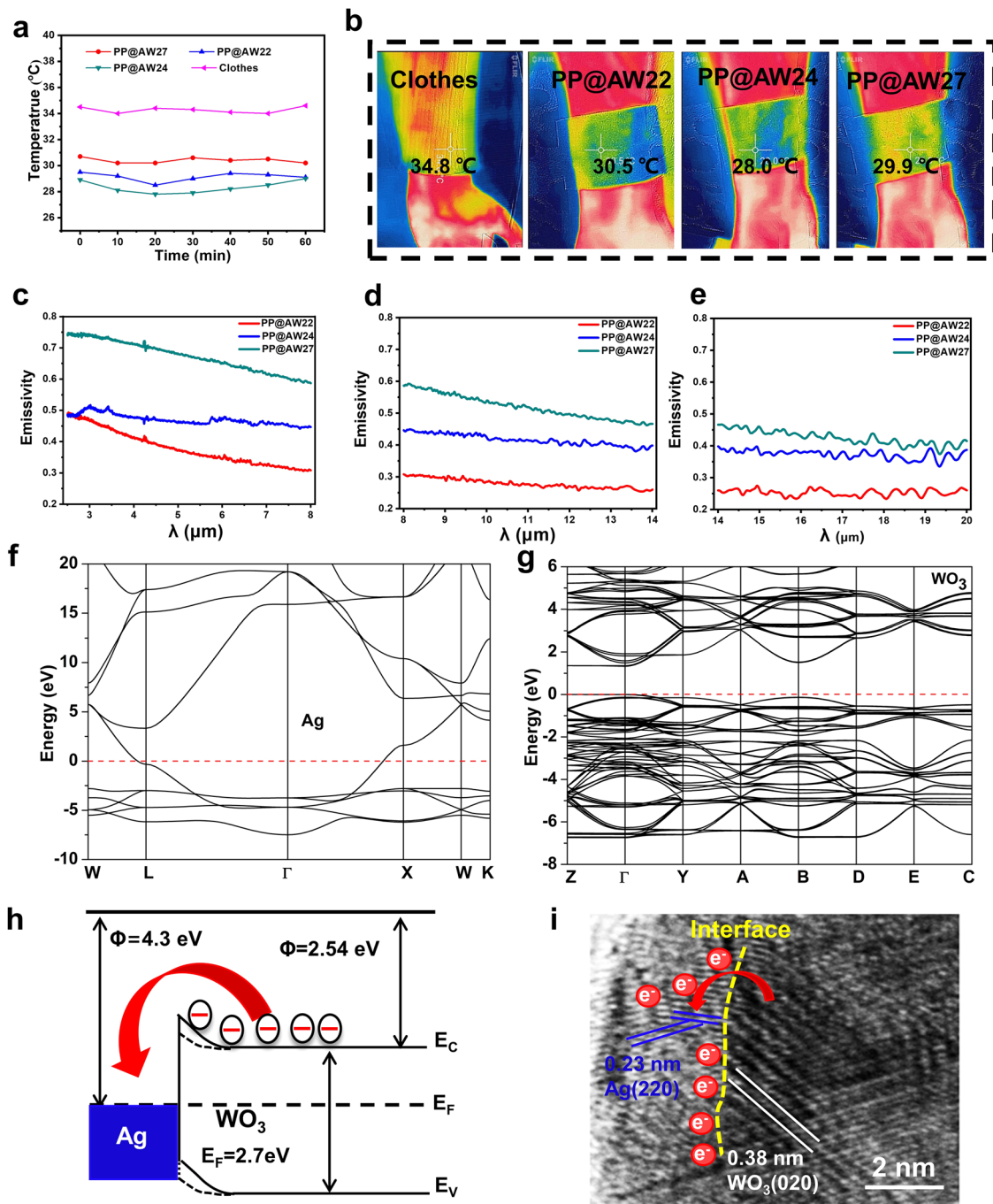


**Fig. 4 IR-stealth properties of PP@AW hybrid membranes.** **a** Changes in temperature of different hybrid membranes placed on the human body as a function of time and **b** IR digital camera images of clothes, and PP@AW22, PP@AW24, and PP@AW27 hybrid membranes placed on a human body. IR emissivity of PP@AW hybrid membranes in **c** near-, **d** medium- and **e** far-infrared bands, respectively. Energy band diagram of **f** Ag and **g**  $WO_3$ . **h** Schematic illustration of the energy diagram and charge-transfer process in Ag- $WO_3$  nanoparticles. **i** Schematic illustration of electron transition when a Schottky junction is formed.

## Methods

**Materials.** PAN (MW = 150,000) and PU (MW = 500,000) were acquired from Jilin Carbon Group while silver nitrate ( $AgNO_3$ ), and dimethyl formamide (DMF) were purchased from Tianjin Tiantai Refine Chemicals Co., Ltd. Sodium tungstate dihydrate ( $Na_2WO_4 \cdot 2H_2O$ ) was purchased from Sinopharm Chemical Reagent Corporation. Sodium hydroxide (NaOH), acetic acid ( $C_2H_4O_2$ ), ethylene glycol ( $C_2H_6O_2$ ), and ammonia solution ( $NH_3 \cdot H_2O$ , 25%) were purchased from Beijing Chemical Works. All the reagents were used as received without further purification.

**Preparation of PAN-PU (PP@ $AgNO_3$ ) nanofibrous membrane via electrospinning.** PAN (1.4 g) was dissolved in 15.46 g of DMF and vigorously stirred at

65 °C for 6 h to form a 8.3 wt.% solution. Meanwhile, 0.39 g of PU was added to 2.2 g of DMF to form a 15 wt.% solution, followed by continuous magnetic stirring at 25 °C for 6 h to form a homogeneous and viscous solution. After cooling down the PAN-DMF solution to room temperature, both solutions were thoroughly mixed to obtain a homogeneous mixture. The addition of PU to the nanofibrous membranes increased their integrity<sup>52</sup>. After stirring the mixed solution for 0.5 h, 0.3 g of  $AgNO_3$  was added to achieve PAN-PU: $AgNO_3$  molar ratio of 10:1<sup>55</sup>. The resultant solution was stirred vigorously for 12 h in dark to obtain the precursor solution for electrospinning, this solution was placed in a glass capillary (with a 1.5 mm diameter spinning jet) and connected to the positive electrode of a high-voltage power supply. Meanwhile, an aluminum foil was connected to the negative electrode and acted as a collector. The distance between the two electrodes was

fixed at 15 cm, and a voltage of 15 kV was applied to fabricate PP/AgNO<sub>3</sub> nanofibrous membranes. The feeding rate of the solution from the syringe was fixed at 1.2 mL h<sup>-1</sup>. The entire device was placed in an environment with a humidity lower than 20% to ensure efficient solvent evaporation.

**Preparation of PP@Ag seed membranes.** The obtained PP/AgNO<sub>3</sub> nanofiber membranes were placed in a solution containing 8.5 g of sodium hydroxide (NaOH) and 240 mL of ethylene glycol (EG) and subjected to a reduction reaction with microwave radiation at 700 W for ~20 s to convert AgNO<sub>3</sub> into Ag nanoparticles on the surfaces of the polymeric nanofibrous membrane (PP@Ag). After this reaction, the color of the membrane changed to brownish yellow, indicating that silver ions were reduced rapidly to silver nanoparticles. The PP@Ag membranes were subsequently cleaned three times with deionized water and ethanol. Finally, the cleaned membranes were dried in a vacuum oven at 60 °C for 12 h.

**In situ synthesis of PAN-PU@Ag-WO<sub>3</sub> (PP@AW) hybrid membranes.** Ag and WO<sub>3</sub> were deposited on a PP@Ag seed membrane via electroless deposition to obtain Ag-WO<sub>3</sub>-decorated PAN-PU nanofibrous hybrid membrane (PP@AW). In a typical experiment, PP@Ag seed membrane (3 × 6 cm<sup>2</sup>) was put in a 190 mL solution containing 0.68 g of AgNO<sub>3</sub> (4 mmol), 2.64 g of Na<sub>2</sub>WO<sub>4</sub> · 2H<sub>2</sub>O (8 mmol), 7 mL NH<sub>3</sub> · H<sub>2</sub>O and 1 mL CH<sub>3</sub>COOH and stirred continuously. The solution was used as a buffer to maintain the pH of this solution at 10.10 (calibrated with a pH meter at 25 °C). Later, a reducing agent consisting of 0.03 mL of N<sub>2</sub>H<sub>4</sub> · H<sub>2</sub>O dissolved in 10 mL deionized water was added into the above mixture drop by drop. The electroless deposition was allowed to continue for 30 min under 60 rpm at 25 °C. Subsequently, the membrane was removed from the reaction system and washed three times with deionized water and ethanol to remove any surface by-products and dried in an oven at 60 °C overnight. AgNO<sub>3</sub> precursor content was fixed and the Ag/W ratio was optimized by varying the amount of Na<sub>2</sub>WO<sub>4</sub> · 2H<sub>2</sub>O precursor in the electroless plating solution. These feed ratios were used to determine sample nomenclature. For example, as described earlier, the sample name with a Ag/W ratio of 2:4 was named PP@AW24. Furthermore, samples with similar structures but different Ag/W ratios were synthesized as listed in the Supplementary Table 1.

**Characterization.** The structural morphology and chemical composition of the synthesized hybrid membranes were analyzed by field-emission scanning electron microscopy (FE-SEM, FEI Nova 450 NanoSEM) and HRTEM (FEI Tecnai G2 F20). Elemental analysis and surface chemistry were evaluated by EDX and XPS (Thermo Scientific ESCALAB250). Raman spectroscopy was used to confirm structural changes in the PP@AW hybrid membranes and their electrical conductivity was measured using four-probe method (RTS-2, Guangzhou Four Probe Technology Co., Ltd) with a source meter (Keithley 2400, United States) with an inter-pin distance of 1 mm. The microwaves shielding capacity for X- (8–12.4 GHz), Ku- (12–18 GHz), and K-bands (18–26.5 GHz) was measured using a 2-port network analyzer (AV3672B-S, China Electronics Technology Instruments Co., Ltd.). The hybrid membranes were cut into rectangular pieces with dimensions slightly larger than 25 × 10, 16 × 8, and 11 × 4 mm<sup>2</sup> to meet the waveguide requirements of the X-, Ku-, and K-bands, respectively. X-ray attenuation properties of the hybrid membranes were measured using a standard spherical ionization chamber (PTW 30005, PTW Co., Ltd, Germany), in which the X-ray source was a Comet MXR-320/26 X-ray tube (Comet Group, Switzerland), the entire testing system was set according to ISO 4037-1:2019<sup>36</sup>. IR emissivity was measured using a Burke infrared spectrometer (BRUKER OPTICS). Alloy content was measured by thermal gravimetric analyze (Pyris 1 TGA, Perkinelmer), and the A/W ratios in the membranes were calculated using the data collected by inductively coupled plasma atomic emission spectrometry (ICP-AES, Agilent 725). Air permeability tests were conducted using a YG461G Fabric digital ventilation meter to evaluate the potential of as-fabricated nanofiber membranes in radiation protection equipment.

## Data availability

The data that support the findings of this study are available from the corresponding author upon reasonable request.

Received: 7 April 2021; Accepted: 10 September 2021;

Published online: 24 September 2021

## References

- Shahzad, F. et al. Electromagnetic interference shielding with 2D transition metal carbides (MXenes). *Science* **353**, 1137–1140 (2016).
- Chen, Y. et al. High-performance epoxy nanocomposites reinforced with three-dimensional carbon nanotube sponge for electromagnetic interference shielding. *Adv. Funct. Mater.* **26**, 447–455 (2016).
- Xie, L.-Q. et al. A highly sensitive dopamine sensor based on a polyaniline/reduced graphene oxide/Nafion nanocomposite. *Chin. Chem. Lett.* **28**, 41–48 (2017).
- Zhao, H. B., Fu, Z. B., Chen, H. B., Zhong, M. L. & Wang, C. Y. Excellent electromagnetic absorption capability of ni/carbon based conductive and magnetic foams synthesized via a green one pot route. *ACS Appl. Mater. Interfaces* **8**, 1468–1477 (2016).
- Wan, Y. J. et al. Anticorrosive, ultralight, and flexible carbon-wrapped metallic nanowire hybrid sponges for highly efficient electromagnetic interference shielding. *Small* **14**, 1800534 (2018).
- Mishra, R. K., Thomas, M., Abraham, J., Joseph, K. & Sabu, T. in *Advanced Materials for Electromagnetic Shielding: Fundamentals, Properties, and Applications* 327–365 (2018).
- Kim, Y., Park, S. & Seo, Y. Enhanced X-ray shielding ability of polymer–nonleaded metal composites by multilayer structuring. *Ind. Eng. Chem. Res.* **54**, 5968–5973 (2015).
- Lee, S. H. et al. Density-tunable lightweight polymer composites with dual-functional ability of efficient EMI shielding and heat dissipation. *Nanoscale* **9**, 13432–13440 (2017).
- Li, M. L., Muneer, B., Yi, Z. X. & Zhu, Q. A Broadband compatible multispectral metamaterial absorber for visible, near-infrared, and microwave bands. *Adv. Opt. Mater.* **6**, 1701238 (2018).
- Zhang, X. A. et al. Dynamic gating of infrared radiation in a textile. *Science* **363**, 619–623 (2019).
- Zhong, S. M. et al. A radar-infrared bi-stealth structure based on metasurfaces. *Appl. Phys. Lett.* **110**, 063502 (2017).
- Bakal, F., Yapici, A., Karaaslan, M. & Akgöl, O. Microwave absorption performance of hexagonal nano boron nitride doped basalt fabric-reinforced epoxy composites. *Aircr. Eng. Aerosp. Technol.* **93**, 205–211 (2021).
- Ozturk, M., Sevim, U. K., Akgöl, O., Unal, E. & Karaaslan, M. Investigation of the mechanic, electromagnetic characteristics and shielding effectiveness of concrete with boron ores and boron containing wastes. *Constr. Build. Mater.* **252**, 119058 (2020).
- Shen, B., Zhai, W., Tao, M., Ling, J. & Zheng, W. Lightweight, multifunctional polyetherimide/graphene@Fe<sub>3</sub>O<sub>4</sub> composite foams for shielding of electromagnetic pollution. *ACS Appl. Mater. Interfaces* **5**, 11383–11391 (2013).
- Zhang, W. et al. Nafion covered core-shell structured Fe<sub>3</sub>O<sub>4</sub>@graphene nanospheres modified electrode for highly selective detection of dopamine. *Anal. Chim. Acta* **853**, 285–290 (2015).
- Chung, D. D. L. Electromagnetic interference shielding effectiveness of carbon materials. *Carbon* **39**, 279–285 (2001).
- Al-Saleh, M. H., Saadeh, W. H. & Sundararaj, U. EMI shielding effectiveness of carbon based nanostructured polymeric materials: a comparative study. *Carbon* **60**, 146–156 (2013).
- Thomassin, J. M. et al. Polymer/carbon based composites as electromagnetic interference (EMI) shielding materials. *Mat. Sci. Eng. R.* **74**, 211–232 (2013).
- Özkan, İ., Duru Baykal, P. & Karaaslan, M. Investigation of electromagnetic shielding properties of metal composite tufted carpets. *J. Textile Inst.* **111**, 476–483 (2020).
- Kumar, R. et al. Recent progress on carbon-based composite materials for microwave electromagnetic interference shielding. *Carbon* **177**, 304–331 (2021).
- Kumar, R. et al. Nitrogen–sulfur co-doped reduced graphene oxide-nickel oxide nanoparticle composites for electromagnetic interference shielding. *ACS Appl. Nano Mater.* **2**, 4626–4636 (2019).
- Kumar, R. et al. Self-assembled nanostructures of 3D hierarchical faceted-iron oxide containing vertical carbon nanotubes on reduced graphene oxide hybrids for enhanced electromagnetic interface shielding. *Compos. Part B. Eng.* **168**, 66–76 (2019).
- Iqbal, A. et al. Anomalous absorption of electromagnetic waves by 2D transition metal carbonitride Ti<sub>3</sub>C<sub>2</sub>T<sub>x</sub> (MXene). *Science* **369**, 446–450 (2020).
- Liu, J. et al. Hydrophobic, flexible, and lightweight mxene foams for high-performance electromagnetic interference shielding. *Adv. Mater.* **29**, 1702367 (2017).
- Cao, W. T. et al. Binary strengthening and toughening of MXene/cellulose nanofiber composite paper with nacre-inspired structure and superior electromagnetic interference shielding properties. *ACS Nano* **12**, 4583–4593 (2018).
- Han, M. et al. Beyond Ti<sub>3</sub>C<sub>2</sub>T<sub>x</sub>: MXenes for electromagnetic interference shielding. *ACS Nano* **14**, 5008–5016 (2020).
- Liang, L. et al. Flexible polyvinylidene fluoride film with alternating oriented graphene/Ni nanochains for electromagnetic interference shielding and thermal management. *Chem. Eng. J.* **395**, 125209 (2020).
- Zhang, Y., Pan, T. & Yang, Z. Flexible polyethylene terephthalate/polyaniline composite paper with bending durability and effective electromagnetic shielding performance. *Chem. Eng. J.* **389**, 124433 (2020).

29. Jin, X. et al. Flame-retardant poly(vinyl alcohol)/MXene multilayered films with outstanding electromagnetic interference shielding and thermal conductive performances. *Chem. Eng. J.* **380**, 122475 (2020).
30. Iqbal, A. et al. Enhanced absorption of electromagnetic waves in  $\text{Ti}_3\text{C}_2\text{Tx}$  MXene films with segregated polymer inclusions. *Compos. Sci. Technol.* **213**, 108878 (2021).
31. Hano, N., Takafuji, M., Noguchi, H. & Ihara, H. Monodisperse surface-charge-controlled black nanoparticles for near-infrared shielding. *ACS Appl. Nano Mater.* **2**, 3597–3605 (2019).
32. Zhang, C. et al. An ultralight and thin metasurface for radar-infrared bi-stealth applications. *J. Phys. D Appl. Phys.* **50**, 444002 (2017).
33. Kim, D. G., Choi, J. H., Choi, D. K. & Kim, S. W. Highly bendable and durable transparent electromagnetic interference shielding film prepared by wet sintering of silver nanowires. *ACS Appl. Mater. Interfaces* **10**, 29730–29740 (2018).
34. Lu, Y. X., Jiang, S. H. & Huang, Y. M. Ultrasonic-assisted electroless deposition of Ag on PET fabric with low silver content for EMI shielding. *Surf. Coat. Tech.* **204**, 2829–2833 (2010).
35. Joshi, A. & Datar, S. Carbon nanostructure composite for electromagnetic interference shielding. *Pramana J. Phys.* **84**, 1099–1116 (2015).
36. Gao, J. F. et al. Flexible, superhydrophobic and highly conductive composite based on non-woven polypropylene fabric for electromagnetic interference shielding. *Chem. Eng. J.* **364**, 493–502 (2019).
37. Liu, C. M. et al. The effect of polydopamine on an Ag-coated polypropylene nonwoven fabric. *Polymers* **11**, 627 (2019).
38. Niklasson, G. A. & Granqvist, C. G. Electrochromics for smart windows: thin films of tungsten oxide and nickel oxide, and devices based on these. *J. Mater. Chem.* **17**, 127–156 (2007).
39. Lu, X. H. et al.  $\text{WO}_3$ -x@Au@MnO<sub>2</sub> core-shell nanowires on carbon fabric for high-performance flexible supercapacitors. *Adv. Mater.* **24**, 938–944 (2012).
40. Inberg, A., Bogush, V., Croitoru, N. & Shacham-Diamanda, Y. Electrochemical study of the mechanism of Ag(W) electroless deposition. *J. Electrochem. Soc.* **154**, D1–D4 (2007).
41. Nambiar, S. & Yeow, J. T. W. Polymer-composite materials for radiation protection. *ACS Appl. Mater. Interfaces* **4**, 5717–5726 (2012).
42. Kim, J., Seo, D., Lee, B. C., Seo, Y. S. & Miller, W. H. Nano-W dispersed gamma radiation shielding materials. *Adv. Eng. Mater.* **16**, 1083–1089 (2014).
43. Aghaz, A. et al. Radiation attenuation properties of shields containing micro and Nano  $\text{WO}_3$  in diagnostic X-ray energy range. *Int. J. Radiat. Res.* **14**, 127–131 (2016).
44. Inberg, A., Bogush, V., Croitoru, N. & Shacham-Diamand, Y. Electrochemical study of the mechanism of Ag (W) electroless deposition. *J. Electrochem. Soc.* **154**, D1 (2006).
45. Lee, S. et al. Alternating-current MXene polymer light-emitting diodes. *Adv. Funct. Mater.* **30**, 2001224 (2020).
46. He, D. et al. Complete-lifecycle-available, lightweight and flexible hierarchical structured  $\text{Bi}_2\text{WO}_6/\text{WO}_3/\text{PAN}$  nanofibrous membrane for X-Ray shielding and photocatalytic degradation. *Adv. Mater. Interfaces* **8**, 2002131 (2021).
47. Liu, J. H. et al. Elevated gamma-rays shielding property in lead-free bismuth tungstate by nanofabricating structures. *J. Phys. Chem. Solids* **112**, 185–189 (2018).
48. Singh, V. P., Badiger, N. M., Chanthima, N. & Kaewkhao, J. Evaluation of gamma-ray exposure buildup factors and neutron shielding for bismuth borosilicate glasses. *Radiat. Phys. Chem.* **98**, 14–21 (2014).
49. Dong, Y. et al. Effects of  $\text{WO}_3$  particle size in  $\text{WO}_3$ /epoxy resin radiation shielding material. *Chin. Phys. Lett.* **29**, 108102 (2012).
50. Azman, N. Z. N., Siddiqui, S. A., Hart, R. & Low, I. M. Effect of particle size, filler loadings and x-ray tube voltage on the transmitted X-ray transmission in tungsten oxide-epoxy composites. *Appl. Radiat. Isotopes* **71**, 62–67 (2013).
51. Li, X. H. & Antonietti, M. Metal nanoparticles at mesoporous N-doped carbons and carbon nitrides: functional Mott-Schottky heterojunctions for catalysis. *Chem. Soc. Rev.* **42**, 6593–6604 (2013).
52. Panda, S. R. & De, S. Preparation, characterization and antifouling properties of polyacrylonitrile/polyurethane blend membranes for water purification. *RSC Adv.* **5**, 23599–23612 (2015).
53. Yao, Y. et al. Ag nanoparticle-sensitized  $\text{WO}_3$  hollow nanosphere for localized surface plasmon enhanced gas sensors. *ACS Appl. Mater. Interfaces* **8**, 18165–18172 (2016).
54. Ji, H. et al. Lightweight and flexible electrospun polymer nanofiber/metal nanoparticle hybrid membrane for high-performance electromagnetic interference shielding. *Npg Asia Mater.* **10**, 749–760 (2018).
55. Song, X. F., Jun, L., Li, Z. Y., Li, S. Y. & Wang, C. Synthesis of polyacrylonitrile/Ag core-shell nanowire by an improved electroless plating method. *Mater. Lett.* **62**, 2681–2684 (2008).
56. Bandalo, V., Greiter, M. B., Bronner, J. & Hoedlmoser, H. ISO 4037:2019 validation of radiation qualities by means of half-value layer and Hp(10) dosimetry. *Radiat. Prot. Dosimetry* **187**, 438–450 (2019).

## Acknowledgements

This work was supported by the research grants from the National Natural Science Foundation of China (No. 21875084), and Jilin Zhenliang Scientific and Technology Company. This work was also partially supported by a grant from the Korea Institute of Science and Technology, the Basic Science Research Program (2017R1A2B3006469 and 2021M3H4A1A03047327) through the National Research Foundation of Korea funded by the Ministry of Science, ICT and Future Planning, and Construction Technology Research Project (19SCIP-B146646-02) funded by the Ministry of Land, Infrastructure and Transport, Republic of Korea.

## Author contributions

C.W., Z.-A.Q., J.-H.Y., and C.-X.J. conceived idea and designed the experiments. D.-Y.H. and N.Z. prepared all the hybrid materials, carried out characterization works, and analyzed microwave shielding data of the nanomaterials, carried out the controlled experiments, and analyzed the data. Y.-Y.M. carried out SEM, and TEM analysis, and IR-stealth experiment. W.W. and H.X. tested mechanical properties and infrared characterization. X.-F.L. performed all the simulations. C.-X.J. was involved in the shielding measurements. R.Z. performed X-ray shielding measurements. N.Z., D.-Y.H., and Z.-A.Q. wrote the paper. X.-F.L. discussed and revised the manuscript. Z.-Q.Z. provided introduction to related applications in clinical medicine. A.I. and C.-M.K. shaped the data and revised the manuscript. C.-M.K. and C.W. supervised the whole project and revised the manuscript.

## Competing interests

The authors declare no competing interests.

## Additional information

**Supplementary information** The online version contains supplementary material available at <https://doi.org/10.1038/s43246-021-00205-3>.

**Correspondence** and requests for materials should be addressed to Chong Min Koo or Ce Wang.

**Peer review information** *Communications Materials* thanks Muharrem Karaaslan and the other, anonymous, reviewer(s) for their contribution to the peer review of this work. Primary Handling Editor: Aldo Isidori. Peer reviewer reports are available.

**Reprints and permission information** is available at <http://www.nature.com/reprints>

**Publisher's note** Springer Nature remains neutral with regard to jurisdictional claims in published maps and institutional affiliations.

 **Open Access** This article is licensed under a Creative Commons Attribution 4.0 International License, which permits use, sharing, adaptation, distribution and reproduction in any medium or format, as long as you give appropriate credit to the original author(s) and the source, provide a link to the Creative Commons license, and indicate if changes were made. The images or other third party material in this article are included in the article's Creative Commons license, unless indicated otherwise in a credit line to the material. If material is not included in the article's Creative Commons license and your intended use is not permitted by statutory regulation or exceeds the permitted use, you will need to obtain permission directly from the copyright holder. To view a copy of this license, visit <http://creativecommons.org/licenses/by/4.0/>.

© The Author(s) 2021